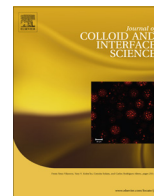




Contents lists available at ScienceDirect

## Journal of Colloid and Interface Science

www.elsevier.com/locate/jcis



# Fluorescent magnetic nanoparticles for cell labeling: Flux synthesis of manganite particles and novel functionalization of silica shell



Michal Kačenka<sup>a,b</sup>, Ondřej Kaman<sup>a,c,\*</sup>, Soňa Kikerlová<sup>c</sup>, Barbora Pavlů<sup>c</sup>, Zdeněk Jiráček<sup>a</sup>, Daniel Jiráček<sup>d,e</sup>, Vít Herynek<sup>d</sup>, Jan Černý<sup>c</sup>, Frédéric Chaput<sup>f</sup>, Sophie Laurent<sup>g</sup>, Ivan Lukeš<sup>b</sup>

<sup>a</sup> Institute of Physics AS CR, Cukrovarnická 10, 162 00 Praha 6, Czech Republic

<sup>b</sup> Department of Inorganic Chemistry, Faculty of Science, Charles University, Albertov 6, 128 43 Praha 2, Czech Republic

<sup>c</sup> Department of Cell Biology, Faculty of Science, Charles University, Albertov 6, 128 43 Praha 2, Czech Republic

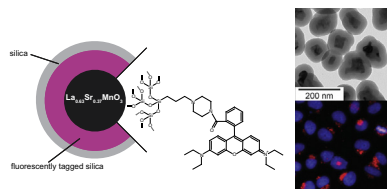
<sup>d</sup> Institute of Clinical and Experimental Medicine, Vídeňská 1958, 140 21 Praha 4, Czech Republic

<sup>e</sup> Institute of Biophysics and Informatics, 1st Faculty of Medicine, Charles University, Kateřinská 32, 121 08 Praha 2, Czech Republic

<sup>f</sup> Laboratoire de Chimie, UMR 5182 ENS-CNRS-UCBL, 46 allée d'Italie, 69364 Lyon cedex 07, France

<sup>g</sup> Department of General, Organic and Biomedical Chemistry, NMR and Molecular Imaging Lab, University of Mons, B-7000 Mons, Belgium

## GRAPHICAL ABSTRACT



## ARTICLE INFO

### Article history:

Received 21 December 2014

Accepted 26 January 2015

Available online 4 February 2015

### Keywords:

Manganites  
Magnetic nanoparticles  
Molten salt synthesis  
Silica coating  
Dual probes  
MRI  
Cell labeling

## ABSTRACT

Novel synthetic approaches for the development of multimodal imaging agents with high chemical stability are demonstrated. The magnetic cores are based on  $\text{La}_{0.63}\text{Sr}_{0.37}\text{MnO}_3$  manganite prepared as individual grains using a flux method followed by additional thermal treatment in a protective silica shell allowing to enhance their magnetic properties. The cores are then isolated and covered *de novo* with a hybrid silica layer formed through the hydrolysis and polycondensation of tetraethoxysilane and a fluorescent silane synthesized from rhodamine, piperazine spacer, and 3-iodopropyltrimethoxysilane. The aminoalkyltrialkoxysilanes are strictly avoided and the resulting particles are hydrolytically stable and do not release dye. The high colloidal stability of the material and the long durability of the fluorescence are reinforced by an additional silica layer on the surface of the particles. Structural and magnetic studies of the products using XRD, TEM, and SQUID magnetometry confirm the importance of the thermal treatment and demonstrate that no mechanical treatment is required for the flux-synthesized manganite. Detailed cell viability tests show negligible or very low toxicity at concentrations at which excellent labeling is achieved. Predominant localization of nanoparticles in lysosomes is confirmed by immunofluorescence staining. Relaxometric and biological studies suggest that the functionalized nanoparticles are suitable for imaging applications.

© 2015 Elsevier Inc. All rights reserved.

## 1. Introduction

Medical and biological applications of magnetic nanoparticles have been extensively investigated over the past two decades. Such particles can be effectively employed as contrast agents in mag-

\* Corresponding author at: Institute of Physics AS CR, Cukrovarnická 10, 162 00 Praha 6, Czech Republic. Fax: +420 233 343 184.

E-mail address: kaman@seznam.cz (O. Kaman).

netic resonance imaging (MRI), not only for diagnostic purposes in human medicine but also in biological research for cell labeling and tracking *in vivo* [1,2]. Similarly, the results of early clinical trials of the use of magnetic nanoparticles in cancer treatment based on magnetically induced hyperthermia are also promising [3]. Furthermore, magnetic nanocarriers offer multiple advantages in bio-separation [4,5] and may provide a vector for targeted drug delivery [6]. With the emergence of more complex nanomaterials that integrate several functional modalities at the nanoscopic level, completely new applications and hybrid techniques have become available. Tremendous progress in bioimaging has been achieved by virtue of multimodal agents that enable the combination of visualization *via* MRI with optical imaging [2,7], imaging based on radioactive isotopes (PET, SPECT) [8], or ultrasound imaging [9].

Various materials have been investigated as prospective magnetic cores for bioapplications, namely, ferro- or ferrimagnetic oxide phases, most commonly iron oxides, *i.e.*, maghemite and magnetite, although ferrites [10,11] and manganites [12–14], etc. have been also studied. Iron oxide nanoparticles are of particular interest, primarily because of their low toxicity and facile synthesis as well as the extensive available knowledge regarding the biological fate of these particles. However, it has been demonstrated that multicomponent oxides may allow for better tuning of magnetic properties for particular applications compared with what can be achieved using simple binary compounds such as iron oxides [15]. An excellent example is the perovskite  $\text{La}_{1-x}\text{Sr}_x\text{MnO}_3$  (LSMO) phase, the Curie temperature of which can be adjusted through modification of the composition and size of the particles to a level suitable for use in the magnetically induced hyperthermia [16]. Upon exceeding the Curie temperature, the particles no longer dissipate energy of an AC magnetic field, and thus, the risk of local overheating is ruled out. Moreover, the high susceptibility of LSMO particles indicates that this material could be useful for a variety of other applications. Recently, a dual MRI/fluorescence contrast agent based on LSMO nanoparticles has been tested for cellular labeling [1,17], and LSMO nanocarriers have been employed for the separation of DNA [4].

LSMO nanoparticles are traditionally prepared *via* various sol-gel methods using citric acid and ethylene glycol (Péchine process) [12,16], amino acids [13,18], or polyvinyl alcohol [19] as the gelifying agents. Unfortunately, single-phase manganite is obtained only after the complex sol-gel precursor is heated to an elevated temperature, typically higher than 650 °C. Consequently, partial sintering begins to occur in the product, and connecting bridges form between grains [20,21]. It is possible to break these connections through harsh mechanical processing. However, such treatment is accompanied by a broadening of the size distribution and the formation of a fraction of very fine fragments [21]. Several other synthetic procedures for LSMO nanoparticles have been reported, namely, the hydrothermal method [22,23], aerosol flame pyrolysis [24], and flux preparation, the so-called molten salt synthesis (MSS) [25,26], but only the last one seems to overcome the drawbacks of sol-gel routes with respect to the morphology and size distribution of the particles. However, LSMO nanoparticles prepared *via* MSS have not yet been tested in highly demanding applications such as those in biology or medicine, and existing reports address solely their magnetic properties and structure [27,28]. In particular, these studies have revealed rather low magnetic moments and reduced Curie temperatures of the as-prepared MSS nanoparticles, but at the same time, it has been demonstrated that the magnetic properties of these particles might be considerably enhanced by post-synthetic annealing (henceforth referred to post-annealing). To prevent the growth of manganite cores and the occurrence of sintering processes at elevated temperature,

post-annealing must be applied after silica coating. Afterwards, the manganite nanoparticles can be easily released through alkaline dissolution of the silica components [27,28]. Hence, post-annealing in silica allows the advantages of flux synthesis to be maintained while improving the magnetic properties of the products.

This contribution reports on the synthesis of a bimodal MRI/fluorescence imaging agent with magnetic cores based on  $\text{La}_{0.63}\text{Sr}_{0.37}\text{MnO}_3$  manganite prepared *via* MSS followed by post-annealing in silica nanoreactors. The magnetic cores are isolated and coated *de novo* with a hybrid silica shell, which incorporates covalently attached rhodamine and exhibits enhanced chemical stability by virtue of its novel aminoalkyltrialkoxysilane-free synthesis. Often, silica layers with covalently attached organic moieties are prepared through the organic derivatization of aminoalkyltrialkoxysilanes, such as 3-aminopropyltriethoxysilane (APS), that are subsequently employed in the coating of particles or for terminal grafting of organic molecules onto their silica surfaces. Alternatively, hybrid silica shell containing aminoalkyl moieties is prepared at first and specifically functionalized afterwards. However, it has been indicated that complex nanoparticles obtained by these traditional procedures show some hydrolytic instability: the dye, although covalently embedded in a silica shell, leaches out of the particles, or an organic corona, originally attached to the particle surface, is gradually released [29–33]. A clear evidence for the hydrolytic deterioration of such organically functionalized nanoparticles was published as early as 1980 [29]. Although systematic studies dealing with the chemical stability of organic functionalization and the specific role of aminoalkyltrialkoxysilanes are very scarce, the underlying mechanism of the hydrolytic instability is not entirely unclear. Bridger and Vincent [29] originally suggested three possible processes that caused the deterioration of their PEGylated nanoparticles: the hydrolysis of the urethane link employed for the attachment of poly(ethylene oxide) to APS, the oxidative degradation of the poly(ethylene oxide) chains, and the dissolution of surface silica layers. The last process is particularly relevant when residual free amino groups are present in the silica shell since the hydrolysis of siloxane bond is a base-catalyzed reaction. Silica matrices containing APS are thus especially prone to hydrolytic processes. Thorough studies of aminopolysiloxanes prepared by the polycondensation of APS and tetraethoxysilane (TEOS) were undertaken by Zhmud and Sonnefeld who evidenced high solubility in water and gradual release of the organic component [34]. Conclusive quantitative data on the stability of materials obtained by grafting APS onto silica were also provided by Etienne and Walcarius [33].

Based on these reports we realized that incomplete conversion of amino groups during the organic functionalization of aminoalkoxysilanes or poor purification of the resulting complex silanes may significantly reduce the hydrolytic stability of the final nanoparticles. However, the type of bonding involved in hybrid silica shells should be also taken into account. The stability of both the hybrid shell and surface anchoring might be seriously impaired if the condensation of alkoxysilanes does not dominate and only adsorption *via* multiple hydrogen bonds occurs instead. This non-covalent adsorption can be easily recognized by instantaneous leaching during purification of the final product and can be prevented by suitable adjustment of reaction conditions [35].

To avoid the use of any aminoalkylsilanes, our synthesis is accomplished through the alkylation of the fluorophore with 3-iodopropyltrimethoxysilane, leading to a complex silane that is isolated and subsequently used in the silica coating procedure of the Stöber's type. The preparation of the fluorescent particles is completed with the application of an additional layer of pure silica

that increases the colloidal stability of the particles in aqueous suspension and protects the rhodamine molecules from any chemical interference from the nanoparticle surroundings. The possible short-term hydrolytic deterioration of the particles is examined, and the observations are compared with previously reported products [17].

## 2. Experimental

### 2.1. Synthesis of RhP

The synthesis of the rhodamine derivative RhP depicted in Scheme 1 was performed under an Ar atmosphere in the dark as follows. Rhodamine B (1.0 g, 2.1 mmol), 4-dimethylaminopyridine (25 mg, 0.2 mmol), and *N*-hydroxysuccinimide (300 mg, 2.6 mmol) were dissolved in anhydrous MeCN (10 ml). Then, a solution of DCC (*N,N*-dicyclohexylcarbodiimide) (1.1 g, 5.3 mmol) in anhydrous MeCN (10 ml) was added dropwise over a duration of 15 min. The resulting mixture was stirred for 5 min and subsequently transferred into a dropping funnel. The activated dye was slowly (over 2 h) added dropwise into a stirred solution of piperazine (1.8 g, 21 mmol) in anhydrous MeCN (20 ml) that had been dissolved beforehand via heating. The reaction mixture was stirred overnight. The white precipitate of dicyclohexylurea was filtered off, and the solution was evaporated on a rotary vacuum evaporator (RVE). The remaining solid material was further treated at 60 °C for 2 h to remove excess of piperazine. The crude product was purified via column chromatography over silica (Merck Silica Gel 60) using MeOH–CHCl<sub>3</sub> (1:5) as the mobile phase. The separation of two dominant components was achieved: the unreacted rhodamine was eluted first, followed by the desired rhodamine derivative. Fractions containing the derivative were combined, evaporated on the RVE and dissolved in a small amount of MeOH. The final product was obtained via precipitation with Et<sub>2</sub>O; the

residue was then washed with Et<sub>2</sub>O and dried. Yield: 400 mg (35%, assuming that the RhP chloride was isolated).

MS (ES, positive): *m/z* (%): 511.5 (100) [(M)<sup>+</sup>]

<sup>1</sup>H NMR (300 MHz, in CD<sub>3</sub>OD): 1.33 (t, *J* = 7.2 Hz, 12 H), 3.12 (br t, *J* = 5.4 Hz, 4 H), 3.63–3.73 (m, 12 H), 6.99 (d, *J* = 2.4 Hz, 2 H), 7.12 (dd, *J* = 9.6 Hz, *J* = 2.4 Hz, 2 H), 7.29 (d, *J* = 9.6 Hz, 2 H), 7.55 (m, 1 H), 7.80 (m, 3 H)

<sup>13</sup>C NMR (75.4 MHz, in CD<sub>3</sub>OD): 12.86, 44.38, 45.61, 46.91, 97.37, 114.80, 115.47, 128.84, 131.40, 131.63, 131.87, 132.41, 133.00, 135.52, 156.62, 157.23, 159.23, 169.49

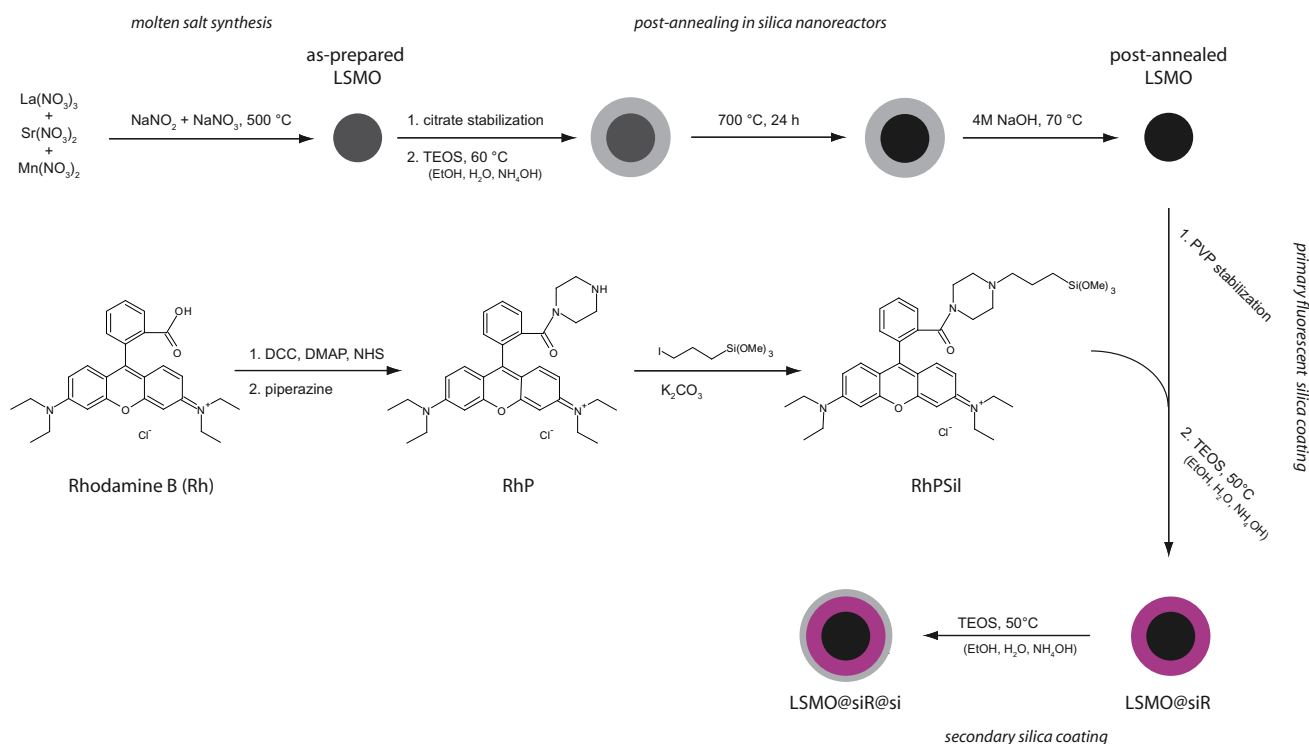
TLC (Merck Silica Gel 60 F<sub>254</sub>; MeOH:CHCl<sub>3</sub> 1:5): *R<sub>f</sub>* = 0.5, magenta spot, (rhodamine B); *R<sub>f</sub>* = 0.25, magenta spot (RhP); *R<sub>f</sub>* = 0.0, mauve spot – ninhydrine detection (piperazine).

### 2.2. Synthesis of RhPSil

The synthesis of RhPSil silane (see Scheme 1) was performed in hydrophobized glass under strictly inert and strictly anhydrous conditions in the dark. Calcined K<sub>2</sub>CO<sub>3</sub> (100 mg, 0.72 mmol) and RhP (25 mg, 46 μmol) were placed under a counter-flow of Ar into a preheated three-necked flask, which was then closed with a rubber septum. Anhydrous MeCN (2.5 ml) was injected, and the RhP dissolved. Thereafter, 3-iodopropyltrimethoxysilane (40 μl, 0.20 mmol) was added via a Hamilton syringe, and the reaction mixture was stirred in the dark for 20 h. Afterwards, the mixture was transferred to an Ar-rinsed syringe and immediately filtered through a PTFE syringe filter into a heart-shaped two-necked flask. The solution was concentrated via evacuation, and the silane was precipitated through the addition of anhydrous Et<sub>2</sub>O. The product was separated via sedimentation and decanted three times with anhydrous Et<sub>2</sub>O. Finally, the product was dried *in vacuo*. Yield: 15 mg (47%, assuming that the RhPSil chloride was isolated).

MS (ES, positive): *m/z* (%): 672.7 (100) [(M)<sup>+</sup>].

<sup>1</sup>H NMR (300 MHz, in CD<sub>3</sub>OD): 0.56–0.66 (m, 2 H), 1.21 (m, 2 H), 1.35 (t, *J* = 7.0 Hz, 12 H), 2.40 (br s, 6 H), 3.45 (br s, 4 H). 3.55 (s,



**Scheme 1.** Overall preparation scheme of fluorescent nanoparticles.

6 H), 3.73 (q,  $J = 7.0$  Hz, 8 H), 7.01 (s, 2 H), 7.12 (d,  $J = 9.6$  Hz, 2 H), 7.31 (d,  $J = 9.6$  Hz, 2 H), 7.53–7.57 (m, 1 H), 7.67–7.84 (m, 3 H).

$^{13}\text{C}$  NMR (75.4 MHz, in  $\text{CD}_3\text{OD}$ ): 7.37, 12.90, 20.37, 41.87, 46.93, 50.95, 53.41, 61.76, 97.35, 114.86, 115.47, 128.89, 131.20, 131.34, 131.65, 132.07, 133.29, 136.62, 156.93, 157.21, 159.27, 169.31.

TLC (Merck Silica Gel 60  $\text{F}_{254}$ ; MeOH:  $\text{CHCl}_3$  1:5):  $R_f = 0.25$ , magenta spot, (RhP);  $R_f = 0.6$ , magenta spot, (RhPSil).

### 2.3. Molten salt synthesis of LSMO cores (as-prepared LSMO)

The starting compounds  $\text{La}(\text{NO}_3)_3 \cdot 6\text{H}_2\text{O}$  ((1 –  $y$ )/9 mmol),  $\text{Sr}(\text{NO}_3)_2$  ( $y$ /9 mmol) and  $\text{Mn}(\text{NO}_3)_2 \cdot 4\text{H}_2\text{O}$  (9 mmol) were mixed with 12.8 g of  $\text{NaNO}_3$ , dissolved in water (50 ml) and evaporated on the RVE. The dry material was thoroughly homogenized in an agate mortar with an additional 10 g of  $\text{NaNO}_3$ . A stainless steel crucible containing 200 g of  $\text{NaNO}_2$  was placed into a shaft furnace preheated to  $\approx 500^\circ\text{C}$ . Once the nitrite had melted completely, mechanical agitation with a stainless steel stirrer was applied, and a thermocouple was inserted between the crucible and the inner furnace wall. After the temperature stabilized at  $490^\circ\text{C}$ , the previously prepared reaction mixture was poured into the molten  $\text{NaNO}_2$  over a duration of approximately 2 min. The flux was stirred while the temperature was maintained for 4 h. Thereafter, the crucible was removed from the furnace, and the molten mixture was quickly poured into a shallow stainless steel dish that was cooled from the bottom with cold water. The solidified mixture was dissolved in 700 ml of water, and the dispersion was left to sediment overnight. After decantation, the solid residue was washed several times with water *via* centrifugation. Subsequent drying *in vacuo* at  $40^\circ\text{C}$  yielded 1.85 g of unpurified LSMO product. The purification emulated the preparatory phase for silica coating (*vide infra*): the particles were agitated in ice-cold 1 M  $\text{HNO}_3$  *via* ultrasound for 15 min and then in ice-cold 0.1 M citric acid, and finally, the particles were washed several times with water. The product was dried *in vacuo* at  $40^\circ\text{C}$ , yielding 1.5 g of the as-prepared LSMO nanoparticles.

### 2.4. Post-annealing in silica nanoreactors and isolation of LSMO cores (post-annealed LSMO)

The unpurified LSMO product (260 mg) was dispersed in EtOH (10 ml) and treated with an ultrasound probe for 1.5 h. Then, the particles were separated *via* centrifugation, washed with water, redispersed in ice-cold 1 M  $\text{HNO}_3$  (12 ml), and treated in an ultrasound bath for 15 min. After centrifugation, the manganite was redispersed in ice-cold 0.1 M citric acid (12 ml), treated again with ultrasound for 15 min, and washed once with water. The particles were redispersed in water (10 ml) with a few drops of ammonia, and the dispersion was treated with an ultrasound probe for 20 min. A mixture of EtOH (300 ml), water (60 ml), and ammonia (20 ml) was prepared in a 500 ml two-neck flask equipped with a PTFE mechanical stirrer; this flask was then placed into an ultrasound bath at a temperature stabilized to  $50^\circ\text{C}$  by a thermostat. The LSMO dispersion was added dropwise to the flask, and the test tube was rinsed with additional water (10 ml). After 10 min, TEOS (1 ml) was added, and the reaction proceeded for 3 h. The coated product was collected *via* centrifugation, washed three times with EtOH and dried. The coated particles were annealed at  $700^\circ\text{C}$  for 24 h. After being allowed to freely cool, the material was mixed with 4 M NaOH (25 ml) in a PTFE crucible and treated at  $\approx 70^\circ\text{C}$  with ultrasound for approximately 1 h. After cooling, the particles were separated *via* centrifugation and redispersed again in fresh 4 M NaOH. Three cycles of such treatment followed. Then, the product was washed three times with water and subjected to

1 M  $\text{HNO}_3$  and 0.1 M citric acid in the same procedure applied prior to the silica coating step (*vide supra*). The overall yield, starting from the unpurified LSMO product and ending with the purified post-annealed cores, was typically 50–60%.

### 2.5. Primary encapsulation of post-annealed LSMO – preparation of LSMO@SiR

Post-annealed LSMO nanoparticles (68 mg) were dispersed in EtOH (10 ml) and treated with an ultrasound probe for 1.5 h. Simultaneously, polyvinylpyrrolidone (PVP) K90 with an average  $M_r \approx 360,000$  (1.4 g) was dissolved in water (130 ml) in a 250 ml round-bottom flask, which was placed into a cooled ultrasound bath, where it was agitated for 30 min. Thereafter, the LSMO suspension was added dropwise, and the mixture was agitated with ultrasound for 12 h. The PVP-stabilized particles were collected *via* centrifugation and washed once with EtOH. Then, the particles were redispersed in EtOH (130 ml) in a 250 ml two-necked flask equipped with a PTFE mechanical stirrer; this flask was then placed into an ultrasound bath at a temperature stabilized to  $50^\circ\text{C}$  by a thermostat. After 20 min of both mechanical and ultrasound agitation, TEOS (100  $\mu\text{l}$ ) was added, followed, after 15 min, by ammonia (19 ml) and, after a further 10 min, by a solution of RhPSil (6 mg) in EtOH (20 ml) followed by additional ammonia (5 ml). After 16 h of stirring and sonication at the given temperature, an additional amount of TEOS (150  $\mu\text{l}$ ) was injected. The process was terminated after 3 h by cooling the mixture in an ice bath. The product was separated *via* centrifugation and washed once with EtOH.

### 2.6. Secondary encapsulation – synthesis of the final LSMO@SiR@Si product

Secondary coating followed immediately after the previous step, and the experimental set-up remained the same. The LSMO@SiR nanoparticles were redispersed in EtOH (150 ml), and TEOS (150  $\mu\text{l}$ ) was then added, later followed by ammonia (24 ml). The ultrasound agitation was terminated after 30 min, after which time the encapsulation mixture was stirred only mechanically for a further 2.5 h. The product was collected *via* centrifugation and was then washed three times with EtOH and four times with water. Heavy fractions were removed through gentle centrifugation (1050 rcf, 10 min) of the diluted water suspension, and the supernatant was isolated as the final product, which was eventually concentrated to a volume of 20 ml. The typical yield with respect to the LSMO weight content was approximately 10%.

### 2.7. Characterization and methods

The synthesized organic compounds RhP and RhPSil were subjected to standard characterization methods, including the acquisition of  $^1\text{H}$  and  $^{13}\text{C}$  NMR spectra, MS with electrospray ionization and TLC; all technical details are provided in the [Supplementary Information](#). The methods employed for the nanoparticles and their suspensions were as follows: XRD, with evaluation of the diffraction patterns *via* the Rietveld method; analysis of the chemical composition of the LSMO cores *via* XRF spectroscopy; SQUID magnetometry; TEM studies of the morphology and size distribution of the particles, supplemented with EDX analysis of their chemical composition; and DLS measurements focused on the colloidal stability and hydrodynamic size of the particles. Finally, AAS chemical analysis was applied to determine the concentrations of manganese in the studied suspensions of nanoparticles. Extensive details regarding the sample preparation and measurements are provided in the [Supplementary Information](#).



## 2.8. Relaxometric, biological, and MRI studies

The longitudinal ( $R_1$ ) and transverse ( $R_2$ ) relaxation rates were determined for the LSMO@SiR@Si product under magnetic fields of  $B = 0.47$  and  $1.41$  T using Bruker Minispec mq20 and mq60 spin analyzers, respectively. The relaxation rates were also observed as a function of the temperature in the range  $15$ – $60$  °C. Preliminary biological experiments were performed using HeLa cells and primary human skin fibroblasts, which were incubated with LSMO@SiR@Si nanoparticles at concentrations of  $c(\text{Mn}) = 10$ – $500$   $\mu\text{mol l}^{-1}$  for 24 h and examined *via* confocal or fluorescence microscopy after thorough rinsing with PBS (Phosphate-Buffered Saline). Cell viability tests were performed using Jurkat cells treated with nanoparticles at concentrations of  $c(\text{Mn}) = 10$ – $2000$   $\mu\text{mol l}^{-1}$  for 48 h, after which time specific staining (Hoechst 33258) of dead cells and flow cytometry were employed for cytotoxicity quantification. The localization of the nanoparticles within cells was studied in HeLa cells incubated with particles at  $c(\text{Mn}) = 10$   $\mu\text{mol l}^{-1}$ , using the immunofluorescence staining of lysosomes targeted by a primary monoclonal antibody against LAMP-1 (Lysosomal-Associated Membrane Protein 1). Finally, a preliminary MRI study was performed, focusing on the labeling of Jurkat cells and their visualization *in vitro*. For this purpose, the incubation proceeded at  $c(\text{Mn}) = 280$   $\mu\text{mol l}^{-1}$  for 24 h, and the thoroughly washed cells were inspected *via* MRI at 4.7 T. All experiments are described in comprehensive detail in the [Supplementary Information](#).

## 3. Results and discussion

### 3.1. Synthesis of the complex fluorescent silane

The complex fluorescent silane RhPSil was synthesized in two steps. In the first step, the coupling of rhodamine B with piperazine was performed, yielding the rhodamine amide RhP, which was then alkylated with 3-iodopropyltrimethoxysilane in the second step (see [Scheme 1](#)). The RhP amide was synthesized *via* a conventional method employing the DCC reagent to prepare the active *N*-hydroxysuccinimidyl ester for subsequent reaction with piperazine. To prevent the possible formation of a double amide of piperazine, the active ester was added dropwise to a large excess of the amine. Although the preparation of RhP from rhodamine B with a yield as high as 70% has previously been reported [36], the advantages of our approach, with a typical yield of 35% after purification *via* column chromatography, include the facile experimental procedures and the use of inexpensive chemicals.

The alkylation of RhP was performed with an excess of 3-iodopropyltrimethoxysilane using  $\text{K}_2\text{CO}_3$  as a base. Because the alkylation agent was a liquid that is well miscible with  $\text{Et}_2\text{O}$ , the product could be easily purified *via* its precipitation with anhydrous  $\text{Et}_2\text{O}$ . The exclusive formation of the monoalkyl derivative was confirmed by the MS spectra, wherein a peak at  $m/z = 672.7$  was recorded but no trace of a double-alkylated derivative was detected. The NMR spectra also indicated the presence of only the monoalkyl derivative. In fact, the integral intensity of the methoxy hydrogen atoms was even lower, being approximately 6 instead of the theoretical value of 9, which was most likely caused by partial hydrolysis of the alkoxy silane moieties, considering that commercial deuterated methanol was used without any drying. This partial hydrolysis also caused some minor peaks in the aliphatic area are present while the integral intensity of the major peaks was somewhat lowered (see the  $^1\text{H}$  NMR spectrum in [Fig. S1 in the Supplementary Information](#)).

To our knowledge, beyond the widely utilized conjugates of rather expensive rhodamineisothiocyanate (RITC) with aminopro-

pyltrialkoxysilanes [37] and a recently published azide-bearing rhodamine derivative [38], this novel silane RhPSil is the only other rhodamine compound that enables direct covalent attachment to silica. Moreover, in the presented synthesis the possible cyclization of the rhodamine B moiety into a lactam form, which exhibits only limited fluorescence, is hindered by the introduction of the secondary amide group [36]. Above all, 3-iodopropyltrimethoxysilane serves as a replacement for traditional aminoalkyltrialkoxysilanes.

### 3.2. Synthesis of LSMO cores

After preliminary experiments with melts of alkali metal nitrates as well as their mixtures and melts thereof that contained additional KOH, our synthetic efforts became focused on molten  $\text{NaNO}_2$  as the most promising flux. Provided that a conservative molar ratio of  $\text{La}:\text{Sr}:\text{Mn} = 1 - y:y:1$  was maintained in the melt, the MSS procedure employing  $\text{NaNO}_2$  flux yielded  $\text{La}_{1-x}\text{Sr}_x\text{MnO}_3$  (with  $x$  well reflecting  $y$ ) nanoparticles after only 1 h of reaction at  $\approx 500$  °C. However, detailed TEM analyses revealed the presence of a considerable amount of amorphous admixture(s) in these products, whose XRD patterns indicated that only a single phase of the rhombohedral perovskite structure was present, without significant evidence of even the typical amorphous “hump”. The compositional analysis of these products *via* XRF yielded evidence of a substantial excess of Mn with respect to the general stoichiometric formula  $\text{La}_{1-x}\text{Sr}_x\text{Mn}_{1+\varepsilon}\text{O}_3$  (for selected samples, see the  $\varepsilon$  values presented in [Table 1](#)). Moreover, experimental annealing of the respective samples at 900 °C for 16 h led to a chemical transformation of the amorphous material that was present, and consequently, hausmannite ( $\text{Mn}_3\text{O}_4$ ) was observed *via* XRD (for illustration, see [Fig. S2 in the Supplementary Information](#)). Finally, the EDX analysis of the amorphous components demonstrated that the predominant metal present in the investigated material was manganese. Therefore, the admixture(s) can be considered to be manganese oxides.

In general, the presence of an amorphous phase suggests that a reaction has not yet been completed (e.g., the mechanism of LSMO synthesis under hydrothermal conditions [39]). Extension of the MSS reaction time to 4 h led to a considerable decrease in the  $\varepsilon$  values of the LSMO products and resulted in a virtual absence of the amorphous phase. Specifically, for the target composition  $\text{La}_{0.63}\text{Sr}_{0.37}\text{MnO}_3$ , which was prepared from a melt with  $y = 0.40$ , a decrease of  $\varepsilon$  to a value of  $-0.07$  (see [Table 1](#)) was observed, which can be interpreted as an indication of either a manganese-deficient perovskite phase or the presence of La- and Sr-rich impurities in the product. However, the XRD patterns of such products often revealed traces of  $\text{SrCO}_3$ . Therefore, mild acid washing with ice-cold diluted  $\text{HNO}_3$  and citric acid was introduced, which eliminated both the traces of  $\text{SrCO}_3$  in the XRD patterns and the manganese sub-stoichiometry (see [Table 1](#)).

Using the prolonged MSS procedure and acidic purification, single-phase LSMO nanoparticles were achieved, which were free of any amorphous admixtures, according to the combined XRD, TEM, and XRF data. Hence, various compositions in the range  $x = 0.18$ – $0.47$  were successfully prepared [27]. Although the reaction took place in molten sodium salt, only a very small amount of Na, never exceeding 2.5 mol% corresponding to the sum of  $\text{Na} + \text{La} + \text{Sr}$ , was observed within a larger series of samples. However, a large number of our experiments conducted under various conditions suggest that some presence of amorphous manganese oxide may be a common problem in the molten salt synthesis of LSMO nanoparticles using alkali metal nitrates and nitrites, if the synthesis procedures are not properly optimized. This problem has not previously been reported; although the preparation of LSMO particles *via* MSS has been attempted in several previous studies [25,26,40,41], sufficient characterization to reveal amor-

**Table 1**  
Chemical compositions of MSS samples prepared under various conditions: the composition of the initial melt is described by parameter  $y$ , the actual composition of the  $\text{La}_{1-x}\text{Sr}_x\text{Mn}_{1+\varepsilon}\text{O}_3$  products is described by stoichiometric parameters  $x$  and  $\varepsilon$ , and  $t$  is the MSS reaction time.

Sample	LSMO from short MSS procedure		Unpurified LSMO	As-prepared LSMO (purified)
$y$	0.5	0.25	0.4	0.4
$t$ (h)	1	1	4	4
Acidic purification	Yes	Yes	No	Yes
$x$	0.46	0.22	0.37	0.37
$1 + \varepsilon$	1.23	1.31	0.93	0.98

phous components has not previously been performed. It is worth noting that Maghsoodi et al. have recently reported the preparation of La-manganite with an intentional excess of Mn via a sol–gel process followed by annealing at 600 °C [42]. The authors presented the XRD patterns of a seemingly single-phase perovskite manganite, but their TEM micrographs clearly revealed the presence of an amorphous phase, which was interpreted as a manganese oxide.

### 3.3. Properties of the as-prepared LSMO cores and post-annealing

The structural and magnetic properties of the as-prepared LSMO nanoparticles in the compositional range  $x = 0.25$ – $0.47$  have been discussed in detail in a separate contribution [28], and therefore, only a brief summary is provided here. The XRD measurements indicated that the nanoparticles exhibited the rhombohedral perovskite structure of the  $R\bar{3}c$  symmetry group, but for higher Sr contents such as  $x = 0.37$ , on which the present study was particularly focused, the structure approached the pseudocubic metrics (the angle  $\alpha_p$  of a simple perovskite subcell is not significantly different from 90°). For the as-prepared nanoparticles, the mean size of the crystallites as evaluated via Rietveld analysis was typically in the range  $d_{\text{XRD}} = 40$ – $50$  nm, and a specific value of  $d_{\text{XRD}} = 45$  nm was determined for the current  $\text{La}_{0.63}\text{Sr}_{0.37}\text{MnO}_3$  sample.

A clear indication of the size and morphology of the nanoparticles is provided by TEM analysis (for illustration, see the TEM micrographs presented in Fig. 1). The as-prepared product consists predominantly of separated and typically cubic-like particles characterized by a rather broad size distribution. The observed mean size of the individual grains roughly corresponds to the  $d_{\text{XRD}}$  values. Although some particles are aggregated or even grown together, a striking feature of the as-prepared LSMO product is the absence of the sintering bridges between grains that arise in nanocrystalline phases prepared via the sol–gel route followed by annealing [43]. Therefore, no mechanical treatment is necessary in the case of MSS nanoparticles.

In a previous study [27], it has been demonstrated that the magnetic properties of as-prepared LSMO nanoparticles deviate from those of comparable sol–gel nanoparticles of similar size, as both the magnetization  $M$  and Curie temperature  $T_C$  were found to be considerably lower for the former. As-prepared  $\text{La}_{0.63}\text{Sr}_{0.37}\text{MnO}_3$  nanoparticles obtained via MSS exhibit  $T_C = 302$  K and  $M_{1000\text{K}/\text{m}}(4.5\text{ K}) = 46.1\text{ Am}^2\text{ kg}^{-1}$ , in contrast with the values of  $T_C = 365$  K and  $M_{1000\text{K}/\text{m}}(4.5\text{ K}) = 64.5\text{ Am}^2\text{ kg}^{-1}$  determined for mechanically treated sol–gel nanoparticles of the same composition and  $d_{\text{XRD}}$  values as small as 28 nm [28]. To elucidate these differences, the magnetic behavior and structure of nanoparticles prepared via MSS have been thoroughly analyzed in a detailed comparative study [28]. The neutron diffraction measurements revealed two important features: the presence of static disorder attributed to random atomic displacements and a surprising coexistence of ferromagnetically ordered regions ( $\mu_{\text{FM}} = 1.98\text{ }\mu_B$  per Mn) and regions with A-type antiferromagnetic alignment ( $\mu_{\text{AFM}} = 1.42\text{ }\mu_B$  per Mn). A possible explanation was found in the effect of a surface layer that exerts compressive stress on the particle interior, which is favorable for the stabilization of the antiferromagnetic phase. It was also demonstrated that the values of both  $T_C$  and  $M$  for the MSS nanoparticles increase upon their annealing at elevated temperatures. Such thermal treatment might suppress the observed static disorder, although it cannot eliminate the antiferromagnetic component.

To enhance the magnetic properties of the nanoparticles while maintaining the advantage of the MSS procedure, namely, the absence of sintering bridges, the as-prepared  $\text{La}_{0.63}\text{Sr}_{0.37}\text{MnO}_3$  nanoparticles were first coated with silica and then subjected to post-annealing at 700 °C for 24 h. The protective silica shell acted as a nanoreactor confining each manganite grain, which was thus prevented from either growing further or forming sintering bridges. The  $d_{\text{XRD}}$  value was found to increase to only 54 nm upon post-annealing, remaining essentially identical to the value observed before the thermal treatment, considering the uncertainty related to the broad size distribution of the crystallites.

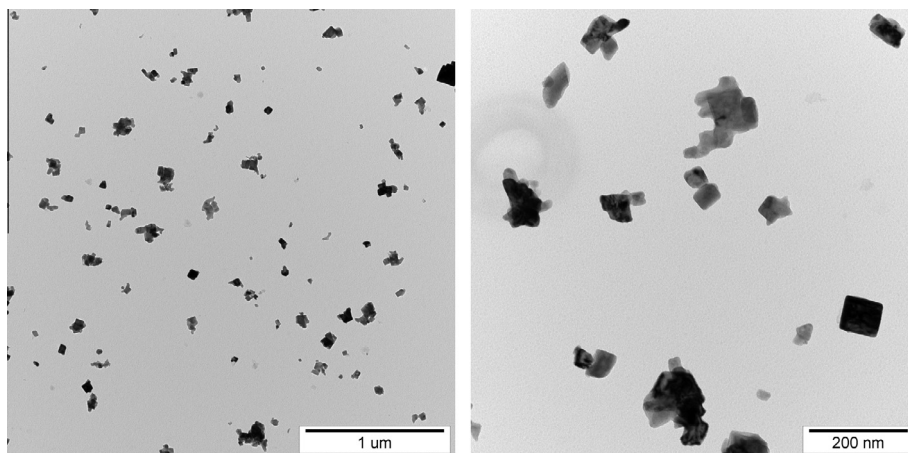


**Fig. 1.** TEM micrographs of as-prepared  $\text{La}_{0.63}\text{Sr}_{0.37}\text{MnO}_3$  cores obtained via MSS.

Finally, all silica components were dissolved via alkaline hydrolysis, and subsequent TEM analysis confirmed that the size of the post-annealed LSMO nanoparticles was indistinguishable from that of the as-prepared sample. At the same time, the Curie temperature increased considerably to  $T_C = 322$  K, and a moderate increase in magnetization to  $M_{1000\text{ kA/m}}(4.5\text{ K}) = 49.1\text{ Am}^2\text{ kg}^{-1}$  occurred upon post-annealing.

### 3.4. Preparation of the complex fluorescent $\text{La}_{0.63}\text{Sr}_{0.37}\text{MnO}_3$ nanoparticles

The general concept of fluorescent magnetic nanoparticles with a two-ply shell was developed based on previous report of FITC-labeled particles [17], but a completely different type of covalent functionalization, free of any aminoalkyltrialkoxysilane, was employed in the present study. The two-ply shell was synthesized via two successive encapsulation procedures (see Scheme 1). In the first step, the post-annealed  $\text{La}_{0.63}\text{Sr}_{0.37}\text{MnO}_3$  cores were coated with rhodamine-tagged silica through the hydrolysis and polycondensation of tetraethoxysilane and RhPSil (preparation of the intermediate product, LSMO@siR). The second encapsulation step was performed employing exclusively TEOS to form an upper layer of pure silica (preparation of the final product, LSMO@siR@si).

The first coating step utilized the PVP method of encapsulation based on the adsorption of polyvinylpyrrolidone on particles, which provides the particles with colloidal stability and facilitates the growth of silica on their surfaces [44]. Importantly, during the first coating procedure, TEOS was added as the first reactant to establish a thin initial layer of pure, more compact silica, whereas RhPSil was added later. The use of a relatively small amount of RhPSil, the formation of the initial silica layer, sufficient stirring, and suitable concentrations of both nanoparticles and organosilanes as well as a fairly long reaction time at the slightly elevated temperature of  $50^\circ\text{C}$  were all found to be crucial for the preparation of well-dispersed LSMO@siR nanoparticles of fine morphology with a reasonable yield, a uniform silica layer, and enough dye embedded in the shell (see the TEM micrographs of LSMO@siR after mild fractionation via centrifugation that are presented in Fig. S3 in the Supplementary Information). The average thickness of the primary, rhodamine-tagged silica shell was 23 nm, and the particles formed a stable dispersion in water. Above all, no rhodamine leaching from the intermediate product LSMO@siR was observed within three weeks of storage in water at laboratory temperature (no longer observation was performed), in contrast to the observation of a rather rapid release of fluorescein moieties from a similar product LSMO@siF, the functionalization of which was based on the derivatization of APS, however, with only an incomplete conversion (the degree of conversion was estimated to be 50% according to  $^1\text{H}$  NMR data) [17].

Despite the above mentioned hydrolytic stability of the prepared product, the two-ply shell architecture was still applied, and the LSMO@siR nanoparticles were further coated with an overlying layer of pure silica. The primary objective of this additional coating was not to enhance the stability of the dye embedding but rather to form a protective silica shell to keep the rhodamine moieties isolated from various potential chemical or even biological (primarily oxidative) effects of the surroundings that might diminish the fluorescence. Moreover, the pure silica layer on the surfaces of the particles shields the positively charged rhodamine moieties and thus restores the negative surface potential through the acidobasic equilibria of silanol groups (partially deprotonated). Hence, the mutual Coulombic repulsion of LSMO@siR@si particles is guaranteed.

The morphology of the final nanoparticles, LSMO@siR@si (see Fig. 2a and b), with their two-ply shells was surprisingly excellent, considering the complexity and multistep nature of the entire syn-

thetic pathway. Image analysis of TEM micrographs, in which the spherical approximation was employed to calculate a diameter from a measured area, indicated that the mean size of an entire LSMO@siR@si nanoparticle was 137 nm and that the mean size of the magnetic core was 70 nm, with standard deviations of 20 and 21 nm, respectively (for histograms of these quantities see Fig. 2c). The thickness of the shell increased by approximately 7 nm compared with LSMO@siR as a result of the secondary silica layer. However, the final particles were not spherical, and this image analysis method underestimates their size, especially in comparison with DLS, which accounts for the entire hydrodynamic diameter. The DLS measurements in pure water were conducted for both the final LSMO@siR@si product and the heavy fraction that was separated during differential centrifugation, and the results clearly illustrates that size fractionation occurred to a certain extent (distributions of DLS intensity are presented in Fig. S4 in the Supplementary Information). The mean hydrodynamic size was found to be  $\approx 200$  nm.

### 3.5. Relaxometric properties

A relaxometric study of the LSMO@siR@si nanoparticles demonstrated that the transverse relaxivity decreases markedly with temperature from  $r_2 = 240\text{ mmol}^{-1}\text{ l s}^{-1}$  at  $15^\circ\text{C}$  to  $85\text{ mmol}^{-1}\text{ l s}^{-1}$  at  $60^\circ\text{C}$  under a magnetic field of  $B = 1.41\text{ T}$  and from  $213\text{ mmol}^{-1}\text{ l s}^{-1}$  to  $53\text{ mmol}^{-1}\text{ l s}^{-1}$  at  $B = 0.47\text{ T}$  (see Fig. 3). The steep temperature dependence of the transverse relaxivity can be attributed to the close vicinity of the Curie temperature  $T_C$ , at which the transition to the paramagnetic state occurs. However, even at temperatures exceeding the value of  $T_C = 322\text{ K}$ , as determined via SQUID magnetometry, the  $r_2$  relaxivity remains quite high, which is clearly caused by the presence of several magnetic cores of larger size and larger  $T_C$ . The well-known relation between the size of a ferromagnetically ordered particle and the temperature of its transition to the paramagnetic state [43] may, therefore, explain the observed temperature dependence in terms of a broad distribution of Curie temperatures of individual magnetic nanoparticles, which is related to the rather broad size distribution [21]. Finally, the values determined for the longitudinal relaxivity are, not surprisingly, very small:  $r_1 \approx 0.3$  and  $0.1\text{ mmol}^{-1}\text{ l s}^{-1}$  at  $B = 1.41\text{ T}$  and  $0.47\text{ T}$ , respectively, in a temperature range of approximately  $20\text{--}40^\circ\text{C}$ .

To conclude this section, we note that the transverse relaxivity at the physiologically relevant temperature  $37^\circ\text{C}$  ( $r_2 = 185$  and  $145\text{ mmol}^{-1}\text{ l s}^{-1}$  at  $B = 1.41\text{ T}$  and  $0.47\text{ T}$ , respectively) is still higher than the typical values reported for contrast agents based on iron oxides [45], suggesting that LSMO might be a useful contrast or labeling agent for  $T_2$ -weighted MR imaging in biological research.

### 3.6. Biological and MRI studies

To investigate the suitability of the fluorescent LSMO@siR@si nanoparticles for further biological studies, preliminary experiments were conducted using cancer-derived, immortalized HeLa cells and primary human skin fibroblasts. Microscopic examination indicated that after incubation, the cells exhibited their standard phenotype, without any observable effect on their size, shape or physiology (see Figs. 4 and S5 in the Supplementary Information). Moreover, numerous dividing HeLa cells were observed at various stages of mitosis to have clearly visible and intact mitotic spindles (see Fig. 4c), providing strong evidence that the LSMO@siR@si nanoparticles did not interfere with the cell cycle. Furthermore, the cytotoxicity was quantitatively assessed using Jurkat cells and flow cytometry analysis. Only very mild toxicity was observed at the highest concentrations of  $c(\text{Mn}) = 1\text{--}2\text{ mmol l}^{-1}$  after 48 h of



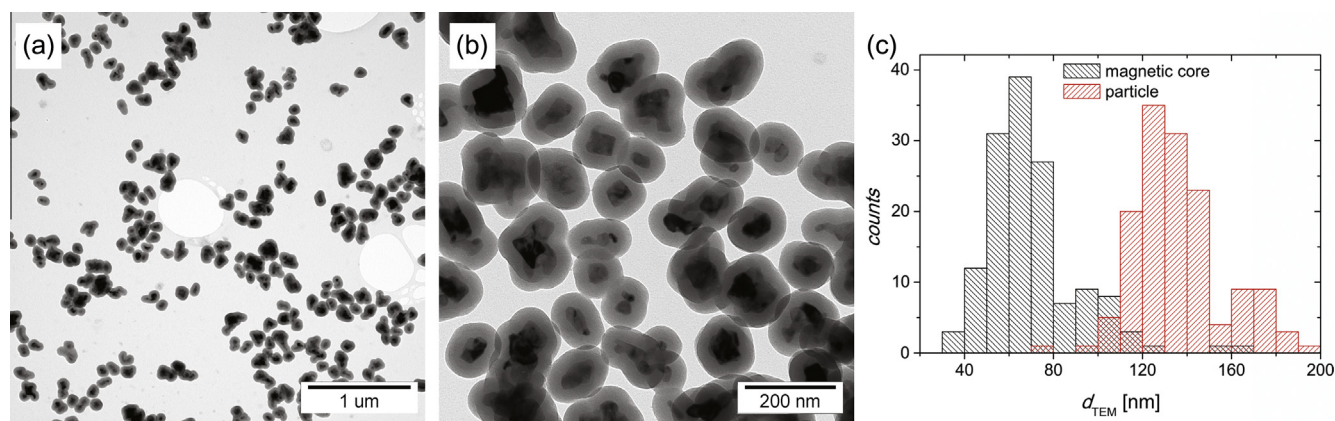


**Fig. 2.** Final LSMO@siR@si nanoparticles possessing two-ply silica shell: (a and b) transmission electron micrographs and (c) size distributions of magnetic cores and whole nanoparticles obtained through the image analysis of the micrographs.

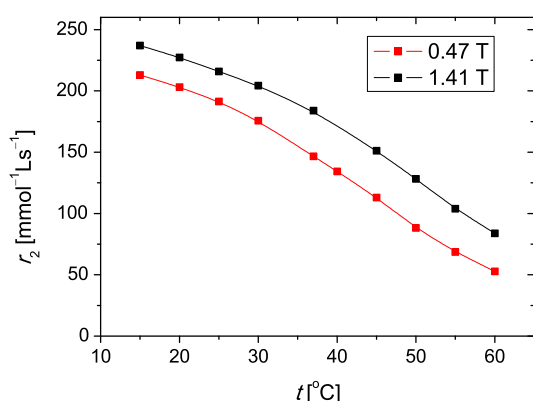


**Fig. 3.** The temperature dependence of the  $r_2$  relaxivity under magnetic fields of 0.47 and 1.41 T for LSMO@siR@si nanoparticles.

incubation (see Figs. 5 and S7 in the Supplementary Information), whereas for lower concentrations, the viabilities were similar to those in control samples that were free of particles.

Confocal microscopy (see Figs. 4a, b and S5 in the Supplementary Information) demonstrated that the nanoparticles were massively internalized into all three types of studied cells. The

fluorescent patterns within the cells resembled the typical distribution of endolysosomal compartment, whereas no particles were dispersed in the cytoplasm or found on the cell surface. Incubation at higher concentrations resulted in the internalization of more particles into the cells, as evidenced by the flow cytometry analysis, according to which the intensity of rhodamine fluorescence in live cells increases with increasing particle concentration (see Fig. 5). Simultaneously, the fluorescence patterns were altered, from dots to small circles. This finding could indicate either significant changes in the geometry of the endolysosomal system or the fact that the particles became somehow associated with the membrane of the compartment. To clarify the intracellular localization of the nanoparticles, the immunofluorescence staining of lysosomes was performed targeting LAMP-1. The HeLa cells were used as a model, and concentrations as low as  $c(\text{Mn}) = 10 \mu\text{mol l}^{-1}$  were applied to avoid overwhelming the endocytic system. The overlays of the nanoparticle fluorescence with the LAMP-1 signal (see Figs. 4 and S6 in the Supplementary Information, and also the sequence of cross sections in video.avi in the online Supplementary Material) confirmed the dominant localization of the LSMO@siR@si nanoparticles within the lysosomes, although a certain proportion of the LAMP-1-positive structures did not seem to contain nanoparticles. Only very rarely the cells have vesicles that contain nanoparticles yet unstained by the anti-LAMP-1 antibody.

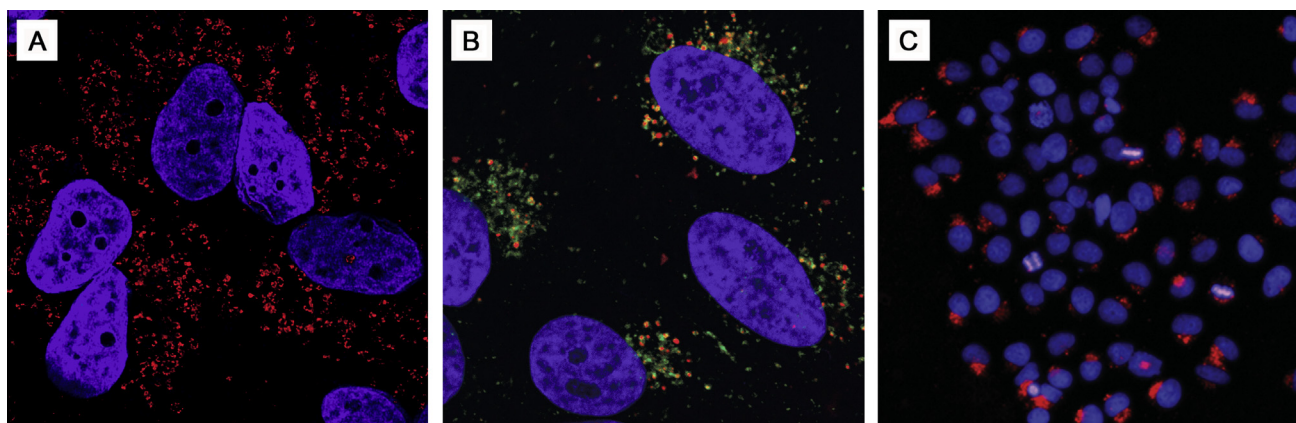


**Fig. 4.** Biological studies of LSMO@siR@si: (a) confocal microscopy image of labeled HeLa cells incubated with LSMO@siR@si at a concentration of  $c(\text{Mn}) = 500 \mu\text{mol l}^{-1}$  for 24 h, (b) confocal microscopy image of HeLa cells with the immunofluorescence staining of lysosomes (primary antibody targeting LAMP1 and secondary antibody labeled by a green fluorescent dye), (c) fluorescence microscopy of HeLa cells incubated with LSMO@siR@si nanoparticles at  $c(\text{Mn}) = 31 \mu\text{mol l}^{-1}$  for 24 h. Different stages of mitosis are visible including intact mitotic spindles. The specimens for microscopy were mounted using a mounting medium that contained DAPI to selectively stain the nuclei (blue), whereas the red signal originated from the rhodamine moieties in the nanoparticles. (For interpretation of the references to color in this figure legend, the reader is referred to the web version of this article.)



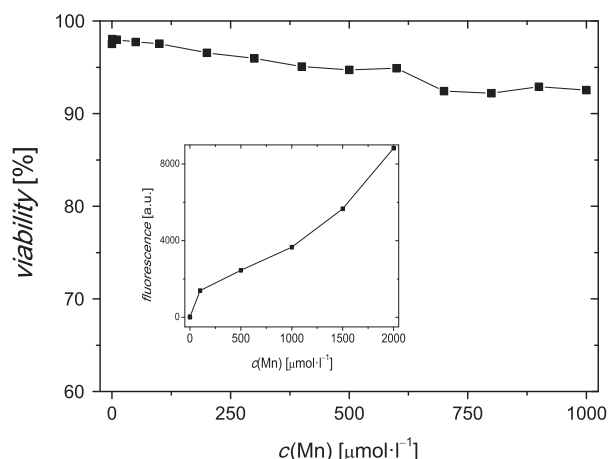


**Fig. 5.** Viability tests of Jurkat cells incubated with LSMO@SiR@Si nanoparticles at various concentrations. The viability quantity denotes the percentage of live cells and was evaluated via the specific staining of dead cells and flow cytometry. The inset presents the intensity of rhodamine fluorescence in life Jurkat cells measured by flow cytometry as function of concentration of nanoparticles in the medium employed for the incubation.

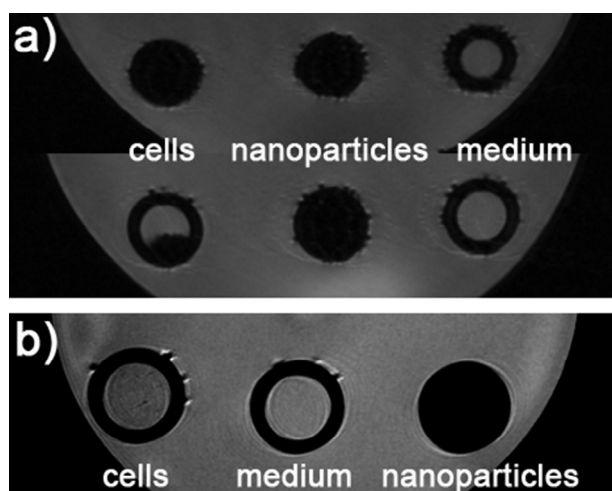


**Fig. 6.**  $T_2$ -weighted MR images of labeled cells, cultivation medium, and a dispersion of LSMO@SiR@Si nanoparticles: (a) two cross-sectional images of centrifuged, labeled cells deposited at the bottom and partially on the wall of an Eppendorf tube (images were acquired at different depths) and (b) samples diluted in 400  $\mu\text{l}$  of 4% gelatine. The cells homogeneously dispersed in the gelatine still exhibited a dark contrast in comparison with the medium in the gel and the water in the surroundings.

Finally, a MRI experiment was performed using Jurkat cells to demonstrate the labeling efficiency of the LSMO@SiR@Si nanoparticles as a  $T_2$  contrast agent. The Jurkat cells were incubated with the nanoparticles at the concentration as low as  $c(\text{Mn}) = 280 \mu\text{mol}\cdot\text{l}^{-1}$  for 24 h, but the negative contrast effect remained very clear in the  $T_2$ -weighted MR images of both cells sedimented via centrifugation and a diluted dispersion of cells in gelatine (see Fig. 6).

#### 4. Conclusions

The major achievements of the present study are related to the synthesis of functionalized silica-coated  $\text{La}_{0.63}\text{Sr}_{0.37}\text{MnO}_3$  manganese nanoparticles with enhanced chemical stability. First, a novel method was employed for the preparation of the cores of these

nanoparticles; this method was based on molten salt synthesis followed by post-annealing in silica nanoreactors. This procedure demonstrated that the mechanical treatment that must be applied to sol-gel products could be avoided through the use of MSS, whereas the post-annealing provided a method for the enhancement of the magnetic properties of the nanoparticles. Second, an increase in the hydrolytic stability of the nanoparticles was accomplished through a two-step derivatization of rhodamine B: its coupling with a piperazine spacer prevented any loss of fluorescence, and its subsequent alkylation with 3-iodopropyltrimethoxysilane enabled its covalent attachment to silica. The traditional approach based on aminoalkyltrialkoxysilanes was thus circumvented, and no leaching of the fluorescent dye was observed. Finally, to protect the rhodamine moieties and to ensure high colloidal stability, a thin secondary silica shell was applied.

Relaxometric studies indicated high transverse relaxivity values of  $r_2 = 145$  and  $185 \text{ mmol}^{-1} \text{ l s}^{-1}$  at  $37^\circ\text{C}$  under magnetic fields of  $B = 0.47 \text{ T}$  and  $1.41 \text{ T}$ , respectively. Furthermore, biological studies revealed no significant toxic effects, even at high concentrations. Extensive internalization by three different cell lines (HeLa cells, Jurkat cells, and primary human fibroblasts) was observed, and the particles did not interfere with the cell cycle. Finally, immunofluorescence staining revealed that the nanoparticles were co-localized predominantly with the lysosomes.

#### Acknowledgments

All authors would like to acknowledge the support of the Czech Science Foundation through project P108/11/0807. Furthermore, I.L. would like to thank the Ministry of Education of the Czech Republic for the support of the LD13012 project; S.K., B.P., and J.C. are grateful to Charles University projects UNCE 204013/2012 and BIOCEV (CZ.1.05/1.1.00/02.0109), from the European Regional Development Fund; and D.J. and V.H. are grateful to the Ministry of Health of the Czech Republic – conceptual development of research organization (Institute for Clinical and Experimental Medicine IKEM, IN00023001). Finally, we would like to thank our colleagues Ondřej Šebesta, for assistance with confocal microscopy and the deconvolution of images, and Jan Blahut, for assistance with NMR measurement.

#### Appendix A. Supplementary data

Supplementary data associated with this article can be found, in the online version, at <http://dx.doi.org/10.1016/j.jcis.2015.01.071>.

#### References

- [1] Z. Berkova, D. Jirak, K. Zacharovova, I. Lukes, Z. Kotkova, J. Kotek, M. Kacenka, O. Kaman, I. Rehor, M. Hajek, F. Saudek, *ChemMedChem* 8 (2013) 614, <http://dx.doi.org/10.1002/cmdc.201200439>.
- [2] Q. Ma, Y. Nakane, Y. Mori, M. Hasegawa, Y. Yoshioka, T.M. Watanabe, K. Gonda, N. Ohuchi, T. Jin, *Biomaterials* 33 (2012) 8486, <http://dx.doi.org/10.1016/j.biomaterials.2012.07.051>.
- [3] B. Thiesen, A. Jordan, *Int. J. Hyperther.* 24 (2008) 467, <http://dx.doi.org/10.1080/02656730802104757>.
- [4] S. Trachtova, O. Kaman, A. Spanova, P. Veverka, E. Pollert, B. Rittich, *J. Sep. Sci.* 34 (2011) 3077, <http://dx.doi.org/10.1002/jssc.201100442>.
- [5] I. Safarik, K. Horska, K. Pospiskova, Z. Maderova, M. Safarikova, *IEEE T Magn* 49 (2013) 213, <http://dx.doi.org/10.1109/tmag.2012.2221686>.
- [6] G.Y. Lee, W.P. Qian, L.Y. Wang, Y.A. Wang, C.A. Staley, M. Satpathy, S.M. Nie, H. Mao, L.L. Yang, *ACS Nano* 7 (2013) 2078, <http://dx.doi.org/10.1021/nn3043463>.
- [7] S.K. Yen, D. Janczewski, J.L. Lakshmi, S. Bin Dolmanan, S. Tripathy, V.H.B. Ho, V. Vijayaragavan, A. Hariharan, P. Padmanabhan, K.K. Bhakoo, T. Sudhaharan, S. Ahmed, Y. Zhang, S.T. Selvan, *ACS Nano* 7 (2013) 6796, <http://dx.doi.org/10.1021/nn401734t>.
- [8] S.M. Kim, M.K. Chae, M.S. Yim, I.H. Jeong, J. Cho, C. Lee, E.K. Ryu, *Biomaterials* 34 (2013) 8114, <http://dx.doi.org/10.1016/j.biomaterials.2013.07.078>.
- [9] Z. Liu, T. Lammers, J. Ehling, S. Fokong, J. Bornemann, F. Kiessling, J. Gatzens, *Biomaterials* 32 (2011) 6155, <http://dx.doi.org/10.1016/j.biomaterials.2011.05.019>.

- [10] J.T. Jang, H. Nah, J.H. Lee, S.H. Moon, M.G. Kim, J. Cheon, *Angewandte Chemie. Int. Ed.* 48 (2009) 1234, <http://dx.doi.org/10.1002/anie.200805149>.
- [11] J. Lu, S.L. Ma, J.Y. Sun, C.C. Xia, C. Liu, Z.Y. Wang, X.N. Zhao, F.B. Gao, Q.Y. Gong, B. Song, X.T. Shuai, H. Ai, Z.W. Gu, *Biomaterials* 30 (2009) 2919, <http://dx.doi.org/10.1016/j.biomaterials.2009.02.001>.
- [12] O. Kaman, E. Pollert, P. Veverka, M. Veverka, E. Hadova, K. Knizek, M. Marysko, P. Kaspar, M. Klementova, V. Grunwaldova, S. Vasseur, R. Epherre, S. Mornet, G. Goglio, E. Duguet, *Nanotechnology* 20 (2009) 094431, <http://dx.doi.org/10.1088/0957-4484/20/27/275610>.
- [13] R. Epherre, E. Duguet, S. Mornet, E. Pollert, S. Louguet, S. Lecommandoux, C. Schatz, G. Goglio, *J. Mater. Chem.* 21 (2011) 4393, <http://dx.doi.org/10.1039/c0jm03963b>.
- [14] K.R. Bhayani, J.M. Rajwade, K.M. Paknikar, *Nanotechnology* 24 (2013) 015102, <http://dx.doi.org/10.1088/0957-4484/24/1/015102>.
- [15] E. Pollert, P. Veverka, M. Veverka, O. Kaman, K. Zaveta, S. Vasseur, R. Epherre, G. Goglio, E. Duguet, *Prog. Solid State Chem.* 37 (2009) 1, <http://dx.doi.org/10.1016/j.progsolidstchem.2009.02.001>.
- [16] S. Vasseur, E. Duguet, J. Portier, G. Goglio, S. Mornet, E. Hadova, K. Knizek, M. Marysko, P. Veverka, E. Pollert, *J. Magn. Mater.* 302 (2006) 315, <http://dx.doi.org/10.1016/j.jmmm.2005.09.026>.
- [17] M. Kačenka, O. Kaman, J. Kotek, L. Falteisek, J. Černý, D. Jiráček, V. Herynek, K. Zacharovová, Z. Berková, P. Jendelova, J. Kupčík, E. Pollert, P. Veverka, I. Lukes, *J. Mater. Chem.* 21 (2011) 157, 039/C0JM01258K.
- [18] O. Pana, R. Turcu, M.L. Soran, C. Leostean, E. Gautron, C. Payen, O. Chauvet, *Synthet. Met.* 160 (2010) 1692, <http://dx.doi.org/10.1016/j.synthmet.2010.06.002>.
- [19] K.P. Shinde, N.G. Deshpande, T. Eom, Y.P. Lee, S.H. Pawar, *Mater. Sci. Eng. B – Adv.* 167 (2010) 202, <http://dx.doi.org/10.1016/j.mseb.2010.02.017>.
- [20] E. Pollert, K. Knizek, M. Marysko, P. Kaspar, S. Vasseur, E. Duguet, *J. Magn. Mater.* 316 (2007) 122, <http://dx.doi.org/10.1016/j.jmmm.2007.02.031>.
- [21] O. Kaman, P. Veverka, Z. Jirak, M. Marysko, K. Knizek, M. Veverka, P. Kaspar, M. Burian, V. Sepelak, E. Pollert, *J. Nanopart. Res.* 13 (2011) 1237, <http://dx.doi.org/10.1007/s11051-010-0117-x>.
- [22] F. Teng, W. Han, S.H. Liang, B.G. Gaugeu, R.L. Zong, Y.F. Zhu, *J. Catal.* 250 (2007) 1, <http://dx.doi.org/10.1016/j.jcat.2007.05.007>.
- [23] J.G. Deng, L. Zhang, H.X. Dai, H. He, C.T. Au, *J. Mol. Catal. A – Chem.* 299 (2009) 60, <http://dx.doi.org/10.1016/j.molcata.2008.10.006>.
- [24] D.J. Babu, A.J. Darbandi, J. Suffner, S.S. Bhattacharya, H. Hahn, *T. Ind. I Met.* 64 (2011) 181, <http://dx.doi.org/10.1007/s12666-011-0035-3>.
- [25] F. Luo, Y.H. Huang, C.H. Yan, S. Jiang, X.H. Li, Z.M. Wang, C.S. Liao, *J. Magn. Mater.* 260 (2003) 173, [http://dx.doi.org/10.1016/S0304-8853\(02\)01317-3](http://dx.doi.org/10.1016/S0304-8853(02)01317-3).
- [26] C. Matei, D. Berger, P. Marote, S. Stoleriu, J.P. Deloume, *Prog. Solid State Chem.* 35 (2007) 203, <http://dx.doi.org/10.1016/j.progsolidstchem.2007.01.002>.
- [27] M. Kačenka, O. Kaman, Z. Jiráček, M. Maryško, P. Žvátora, S. Vratislav, I. Lukeš, *J. Appl. Phys.* 115 (2014) 17B525, <http://dx.doi.org/10.1063/1.4867958>.
- [28] M. Kačenka, O. Kaman, Z. Jiráček, M. Maryško, P. Veverka, M. Veverka, S. Vratislav, *J. Solid State Chem.* 221 (2015) 364, <http://dx.doi.org/10.1016/j.jssc.2014.10.024>.
- [29] K. Bridger, B. Vincent, *Eur. Polym. J.* 16 (1980) 1017, [http://dx.doi.org/10.1016/0014-3057\(80\)90185-8](http://dx.doi.org/10.1016/0014-3057(80)90185-8).
- [30] Z.K. Zhang, A.E. Berns, S. Willbold, J. Buitenhuis, *J. Colloid Interf. Sci.* 310 (2007) 446, <http://dx.doi.org/10.1016/j.jcis.2007.02.024>.
- [31] J.R. Jezorek, K.H. Faltynski, L.G. Blackburn, P.J. Henderson, H.D. Medina, *Talanta* 32 (1985) 763, [http://dx.doi.org/10.1016/0039-9140\(85\)80180-6](http://dx.doi.org/10.1016/0039-9140(85)80180-6).
- [32] M. Gimpel, K. Unger, *Chromatographia* 16 (1982) 117, <http://dx.doi.org/10.1007/BF02258881>.
- [33] M. Etienne, A. Walcarius, *Talanta* 59 (2003) 1173, [http://dx.doi.org/10.1016/S0039-9140\(03\)00024-9](http://dx.doi.org/10.1016/S0039-9140(03)00024-9).
- [34] B. Zhmud, J. Sonnefeld, *J. Non-Cryst. Solids* 195 (1996) 16, [http://dx.doi.org/10.1016/0022-3093\(95\)00497-1](http://dx.doi.org/10.1016/0022-3093(95)00497-1).
- [35] I.J. Bruce, T. Sen, *Langmuir* 21 (2005) 7029, <http://dx.doi.org/10.1021/la050553t>.
- [36] T. Nguyen, M.B. Francis, *Org. Lett.* 5 (2003) 3245, <http://dx.doi.org/10.1021/O1035135z>.
- [37] K.S. Park, J. Tae, B. Choi, Y.S. Kim, C. Moon, S.H. Kim, H.S. Lee, J. Kim, J. Kim, J. Park, J.H. Lee, J.E. Lee, J.W. Joh, S. Kim, *Nanomed.-Nanotechnol.* 6 (2010) 263, <http://dx.doi.org/10.1016/j.nano.2009.07.005>.
- [38] W.J. Zhang, Y.X. Zhang, X.H. Shi, C. Liang, Y.Z. Xian, *J. Mater. Chem.* 21 (2011) 16177, <http://dx.doi.org/10.1039/C1jm12353j>.
- [39] C. Bernard, B. Durand, M. Verelst, P. Lecante, *J. Mater. Sci.* 39 (2004) 2821, <http://dx.doi.org/10.1023/b:jmsc.0000021459.24971.91>.
- [40] J.P. Deloume, J.P. Scharff, P. Marote, B. Durand, A. Abou-Jalil, *J. Mater. Chem.* 9 (1999) 107, <http://dx.doi.org/10.1039/a805309j>.
- [41] Y. Tian, D.R. Chen, X.L. Jiao, *Chem. Mater.* 18 (2006) 6088, <http://dx.doi.org/10.1021/cm0622349>.
- [42] S. Maghsoudi, J. Towfighi, A. Khodadadi, Y. Mortazavi, *Chem. Eng. J.* 215 (2013) 827, <http://dx.doi.org/10.1016/j.cej.2012.11.005>.
- [43] P. Zvátora, M. Veverka, P. Veverka, K. Knizek, K. Zaveta, E. Pollert, V. Kral, G. Goglio, E. Duguet, O. Kaman, *J. Solid State Chem.* 204 (2013) 373, <http://dx.doi.org/10.1016/j.jssc.2013.06.006>.
- [44] C. Graf, D.L.J. Vossen, A. Imhof, A. van Blaaderen, *Langmuir* 19 (2003) 6693, <http://dx.doi.org/10.1021/La0347859>.
- [45] S. Laurent, D. Forge, M. Port, A. Roch, C. Robic, L. Vander Elst, R.N. Muller, *Chem. Rev.* 108 (2008) 2064, <http://dx.doi.org/10.1021/cr068445e>.